

8. Bierman PJ, Vose JM, Leichner PK, et al. Yttrium 90-labeled antiferritin followed by high-dose chemotherapy and autologous bone marrow transplantation for poor-prognosis Hodgkin's disease. *J Clin Oncol* 1993;11:698-703.
9. DeNardo SJ, Kukis DL, Kroger LA, et al. Synergy of Taxol and radioimmunotherapy with yttrium-90-labeled chimeric L6 antibody: efficacy and toxicity in breast cancer xenografts. *Proc Natl Acad Sci USA* 1997;94:4000-4004.
10. Ali MS, Quadri SM. Maleimido derivatives of diethylenetriaminepentaacetic acid and triethylenetetraaminehexaacetic acid: their synthesis and potential for specific conjugation with biomolecules. *Bioconjug Chem* 1996;7:576-583.
11. Mardirossian G, Wu C, Hnatowich DJ. The stability in liver homogenates of indium-111 and yttrium-90 attached to antibody via two popular chelators. *Nucl Med Biol* 1993;20:65-74.
12. Kozak RW, Raubitschek A, Mirzadeh S, et al. Nature of the bifunctional chelating agent used for radioimmunotherapy with yttrium-90 monoclonal antibodies: critical factors in determining in vivo survival and organ toxicity. *Cancer Res* 1989;49:2639-2644.
13. Stimmel JB, Stockstill ME, Kull FC. Yttrium-90 chelation properties of tetraazetatetraacetic acid macrocycles, diethylenetriaminepentaacetic acid analogues, and a novel terpyridine acyclic chelator. *Bioconjug Chem* 1995;6:219-225.
14. Schott ME, Schlom J, Siler K, et al. Biodistribution and preclinical radioimmunotherapy studies using radiolanthanide-labeled immunoconjugates. *Cancer* 1994;73(suppl):993-998.
15. Moi MK, Meares CF, DeNardo SJ. The peptide way to macrocyclic bifunctional chelating agents: synthesis of 2-(p-nitrobenzyl)-1,4,7,10-tetraazacyclododecane-N'-N'',N''',N''''-tetraacetic acid and study of its yttrium (III) complex. *J Am Chem Soc* 1988;110:6266-6267.
16. Harrison A, Walker CA, Parker D, et al. The in vivo release of <sup>90</sup>Y from cyclic and acyclic ligand-antibody conjugates. *Int J Radiat Appl Instrum B* 1991;18:469-476.
17. DeNardo GL, Kroger LA, DeNardo SJ, et al. Comparative toxicity studies of yttrium-90 MX-DTPA and 2-IT-BAD conjugated monoclonal antibody (BrE-3). *Cancer* 1994;73(suppl):1012-1022.
18. Li M, Meares CF, Zhong GR, Miers L, Xiong CY, DeNardo SJ. Labeling monoclonal antibodies with <sup>90</sup>yttrium- and <sup>111</sup>indium-DOTA chelates: a simple and efficient method. *Bioconjug Chem* 1994;5:101-104.
19. Wu C, Brechbiel MW, Kozak RW, Gansow OA. Metal-chelate-dendrimer-antibody constructs for use in radioimmunotherapy and imaging. *Bioorg Med Chem* 1994;4:449-454.
20. Chakrabarti MC, Le N, Paik CH, De Graff WG, Carrasquillo JA. Prevention of radiolysis of monoclonal antibody during labeling. *J Nucl Med* 1996;37:1384-1388.
21. Epstein AL, Marder RJ, Winter JN, et al. Two new monoclonal antibodies, Lym-1 and Lym-2, reactive with human-B-lymphocytes and derived tumors, with immunodiagnostic and immunotherapeutic potential. *Cancer Res* 1987;47:830-840.
22. Liu AY, Robinson RR, Hellström KE, Murray EDJ, Chang CP, Hellström I. Chimeric mouse-human IgG1 antibody that can mediate lysis of cancer cells. *Proc Natl Acad Sci USA* 1987;84:3439-3443.
23. Beaumier PL, Neuzil D, Yang HM, et al. Immunoreactivity assay for labeled anti-melanoma monoclonal antibodies. *J Nucl Med* 1986;27:824-828.
24. DeNardo SJ, Zhong G-R, Salako Q, Li M, DeNardo GL, Meares CF. Pharmacokinetics of chimeric L6 conjugated to <sup>111</sup>In and <sup>90</sup>Y DOTA-peptide in tumor bearing mice. *J Nucl Med* 1995;36:829-836.
25. DeNardo SJ, Peng J-S, DeNardo GL, Mills SL. Immunochemical aspects of monoclonal antibodies important for radiopharmaceutical development. *Nucl Med Biol* 1986;13:303-310.
26. Kukis DL, DeNardo GL, DeNardo SJ, et al. Effect of the extent of chelate substitution on the immunoreactivity and biodistribution of 2IT-BAT-Lym-1 immunoconjugates. *Cancer Res* 1995;55:878-884.
27. Coursey BM, Calhoun JM, Cessna JT. Radioassays of yttrium-90 used in nuclear medicine. *Nucl Med Biol* 1993;20:693-699.
28. Salako QA, DeNardo SJ. Radioassay of yttrium-90 radiation using the radionuclide dose calibrator. *J Nucl Med* 1997;38:723-726.
29. McCall MJ, Diril H, Meares CF. Simplified method for conjugating macrocyclic bifunctional chelating agents to antibodies via 2-iminothiolane. *Bioconjug Chem* 1990;1:222-226.
30. Li M, Meares CF. Synthesis, metal chelate stability studies, and enzyme digestion of a peptide-linked DOTA derivative and its corresponding radiolabeled immunoconjugates. *Bioconjug Chem* 1993;4:275-283.
31. Meares CF, McCall MJ, Reardan DT, Goodwin DA, Diamanti CI, McTigue M. Conjugation of antibodies with bifunctional chelating agents: isothiocyanate and bromoacetamide reagents, methods of analysis, and subsequent addition of metal ions. *Anal Biochem* 1984;142:68-78.
32. DeNardo GL, Mills SL, Kukis DL, Anderson V, DeNardo SJ. Review of a four-year experience iodinating monoclonal antibodies with therapeutic amounts of I-131. *Antibody Immunocnj Radiopharm* 1995;8:1-10.
33. DeNardo SJ, DeNardo GL, Peng JS. Pharmaceutical quality control of radiolabeled monoclonal antibodies and their fragments. *Am J Physiol Imag* 1989;4:39-44.
34. Vriesendorp HM, Quadri SM, Jaeckle KA, Freedman RS, Cromeens DM. Proposal for translational analysis and development of clinical radiolabeled immunoglobulin therapy. *Radiother Oncol* 1996;41:151-161.

## Quantifying the Radiation Dosage to Individual Skeletal Lesions Treated with Samarium-153-EDTMP

Ado J. van Rensburg, Albert S. Alberts and Werner K.A. Louw

Department of Radiation Oncology, Pretoria Academic Hospital, and Atomic Energy Corporation of South Africa Ltd., Pretoria, South Africa

Samarium-153-ethylenediaminetetramethylenephosphonate (EDTMP) is used in the treatment of painful skeletal lesions. This study attempted to quantify the radiation dosage to individual lesions on both the macroscopic and microscopic level. **Methods:** A gamma camera-based quantification technique was adapted and refined for <sup>153</sup>Sm. The accuracy of the technique was determined by using a realistic phantom. The activity and volume of lesions as well as normal bone were determined and used to estimate the radiation dosages to these regions. Two patients died of unrelated causes shortly after receiving <sup>153</sup>Sm-EDTMP. This made it possible to compare the gamma camera results with direct measurements. It also allowed for autoradiographic examination of the lesions. Finally, the microscopic radiation dosages were estimated. **Results:** The phantom study indicated that the quantification technique was off, on average, by 4.1% (s.d. = 8.1%). The absolute activity concentration of trabecular bone was found to be ~0.22 MBq/g, and that of cortical bone was found to be ~0.1 MBq/g, regardless of the dosage administered. The corresponding concentrations for lesions were between 3 and 7 times higher than that of normal bone, with no apparent ceiling. From these results, the macroscopic radiation

dosage could be estimated. The dosage to normal bone varied between 0.9 and 3.9 cGy · kg/MBq, and that of the lesions varied between 5.2 and 27.1 cGy · kg/MBq. The autopsy results confirmed that the gamma camera technique was accurate. The autoradiography showed clearly that the activity was associated with the surface of the bone. From these findings, the microscopic radiation dosage distribution was estimated for cortical and trabecular bone as well as osteoblastic lesions. The variation in the microscopic dosage compared to the macroscopic dosage was quite large. Microscopic dosages, when compared to the macroscopic dosages, were as high as 965% and as low as 14.9%. **Conclusion:** The techniques used have been proven to be accurate. The activity in normal bone may be at a ceiling value for all the administered doses, which could explain the small variation. This is not true for the lesions. The large variation in dosages on a microscopic scale, combined with the ceiling in normal bone, may explain the lower than expected toxicity and relatively quick relapse of the patients.

**Key Words:** samarium-153-EDTMP; quantification; radiation dosimetry

*J Nucl Med* 1998; 39:2110-2115

Received Oct. 2, 1997; revision accepted Mar. 24, 1998.

For correspondence or reprints contact: Ado J. van Rensburg, PhD, Department of Radiation Oncology, Private Bag X169, Pretoria, 0001, South Africa.

Samarium-153-ethylenediaminetetramethylenephosphonate (EDTMP) has been used with good results in the palliation of

painful metastases to bone (1–4). This study forms part of the ongoing quest to find an optimal dose schedule that will give maximal palliation with acceptable toxicity. To date, the radiation dosages have been estimated from basic principles (5–7). Certain assumptions are made as to the percentage of activity taken up by normal bone, as well as the distribution of the activity in the bone. These values are based on studies of healthy animals.

The results of the clinical studies (1–3) showed that the toxicity was lower than expected from these estimates. Combined with the fact that the palliation was of shorter duration than expected, the accuracy of the dose estimates can be questioned.

The aims of this study were:

1. To develop a technique to accurately quantify the activity in the individual lesions as well as in normal bone;
2. To determine the microscopic distribution of the activity;
3. To arrive at the absolute radiation dosage on the microscopic level.

Knowing the radiation dosages to this degree will assist in determining an optimal schedule.

The technique used to determine the in vivo distribution was developed by van Rensburg et al. (8) and Pretorius et al. (9). It uses a channel ratio (CR) to eliminate scatter, combined with geometric mean with attenuation correction (GMA) of parallel opposing gamma camera views. The technique first had to be calibrated for use with  $^{153}\text{Sm}$ . It was then applied to several patients. Although quantitative SPECT has already been used as a basis for dosimetry (10,11), it was not considered because the small size and diffuse nature of the lesions and the uncertainty in density did not justify the added complexity. It was concluded that planar imaging techniques would give sufficient accuracy, based on the previous results of van Rensburg et al. (12).

There is no animal or laboratory model to study the microscopic distribution of  $^{153}\text{Sm}$ -EDTMP in metastases and lesions. The only way to do this, therefore, was to find suitable human material. At the same time, the accuracy of the gamma camera technique could be assessed.

Finally, dose calculations were based on the information gleaned from the preceding investigations to accurately determine the radiation dosages to the lesions and normal bone on both the macroscopic and microscopic level.

## MATERIALS AND METHODS

### Calibration of the Channel Ratio Quantification Technique

The CR quantification technique is described fully elsewhere (9). In short, two half-sized windows (10%) straddling the photopeak are defined. The ratio of the counts in these peaks, when no scatter is present, is denoted G and should be close to 1. It varies across the face of the camera and with the tuning of the camera.

When scatter is present, the ratio between the windows changes. The CR quantification technique is based on the theoretical assumption that the ratio of the scattered components in these two windows remains constant. This ratio is called H and remains close to 3 over a wide range of conditions. The parameters G and H are determined for the study in question. When these values are known, the scattered component can be eliminated using simple mathematics. Here, the G and H values for  $^{153}\text{Sm}$  were calculated from attenuation curves.

*Attenuation Curve Measurement.* Three circular flat sources, 2 mm thick, with diameters of 50, 90 and 155 mm, were filled with a known amount of  $^{153}\text{Sm}$  (~5, 10 and 20 MBq respectively). The sources were imaged in air 65 mm away from an Elscint gamma

camera using a low-energy, all-purpose collimator. A series of images was subsequently collected at various depths of water (0–200 mm) using a specially constructed water bath. The bottom of the water bath was also kept 65 mm away from the face of the camera. Each image in this series consisted of a set acquired with two adjacent windows of 10%, each straddling the peak of  $^{153}\text{Sm}$ . The images were collected in a  $128 \times 128$  word matrix. A circular region of interest (ROI) was drawn to fully enclose the source image at the greatest depth. Because the size of the ROI is critical (12), the size of the ROI was judged visually, as one would in a clinical setting, and was kept constant for all images of one source size. The total counts inside the ROI for both windows were determined at all depths. The counts were then expressed as a percentage of the respective counts at 0 mm, normalized to the surface.

*Determination of G and H Values of the CR Technique.* The parameters H and G that were needed for the CR technique were determined (9) before scatter correction could be performed. A point source placed in front of the open camera face was used to optimize window placing and to ensure that G is close to 1. The data from the attenuation curves were used to calculate H.

*Phantom Quantification.* A hollow phantom was constructed from Plexiglas in the shape of a standard 70-kg man. The external anatomy was realistic and was achieved by vacuum-forming the Plexiglas using plaster of paris casts. The lumbar spine, pelvis and femur bones of a cadaver were placed in position inside the phantom, which was then filled with water. Lesions were simulated by drilling holes in the spine and femurs of 10- and 20-mm diameters. These holes were lined with plastic wrap and filled with a mixture of plaster of paris and water containing known amounts of activity. The ratio of water to plaster of paris was chosen to give a realistic density to the lesions.

The  $^{153}\text{Sm}$  activity of 25 MBq (volume of <3 ml) was measured accurately (error of <2%) in a source calibrator (Picker Isotope Calibrator). The syringe was then imaged in a water-equivalent plastic block at a depth of 50 mm using the two windows on the photopeak setting. The activity remaining behind after the lesions were made was also measured.

Posterior and anterior images of the regions with lesions were collected again using two windows. Regions of interest were drawn, and the counts in the ROIs were noted. A background ROI was also generated for each lesion. A flat, uniform  $^{57}\text{Co}$  source was then used to get a transmission image of the same areas. There was some cross-talk from  $^{153}\text{Sm}$  (103 keV) in the  $^{57}\text{Co}$  (122 keV) window, which was subtracted.

The counts expected for each lesion were determined by correcting the 50-mm measured value of the syringe for scatter, attenuation and activity remaining after use. The equivalent thicknesses at the sites of the lesions were determined from the  $^{57}\text{Co}$  measurements by comparison with the  $^{57}\text{Co}$  attenuation curve. Finally, the CR correction, background subtraction and GMA quantification were performed. In GMA quantification, the square root of the product of the anterior and posterior counts (geometric mean) is taken. This value is then corrected for the attenuation by making use of the equivalent thickness and the appropriate attenuation coefficient (9,12). The study was repeated three times.

### Patient Measurements

The method described above was used to determine the activity in normal bone as well as lesions for patients treated with  $^{153}\text{Sm}$ -EDTMP. Suitable patients were picked from a pool of patients receiving first-time  $^{153}\text{Sm}$ -EDTMP therapy (13).

*Gamma Camera Imaging.* Due to the production cycle of the supplier, the  $^{153}\text{Sm}$ -EDTMP was administered on Fridays. Gamma camera imaging was performed on the following Mondays. A set of

parallel opposing images was collected, usually in the pelvic region. Dual-window settings allowed CR correction to be performed. A transmission image was also collected of the same area. The counts in a region of normal bone as well as a lesion were determined by appropriate ROIs.

The CR correction was applied, background was subtracted and GMA values were calculated to find the total activity of the sample with the aid of a standard source. The volume of the sample was estimated from the sizes of the ROIs.

### Postmortem Investigations

To calculate the radiation dosages on a microscopic level, the distribution of the activity within normal bone and lesions had to be investigated. No animal model of skeletal lesions was readily available. The Institutional Review Board was therefore approached with a proposal to administer  $^{153}\text{Sm}$ -EDTMP to terminal patients on an informed consent basis. This proposal was granted, and postmortem autopsies were performed on two patients who received  $^{153}\text{Sm}$ -EDTMP immediately before death. One of the patients, who had primary lung adenosquamous cancer, was also used to assess the gamma camera quantification technique.

**Gamma Camera Investigation.** The normal gamma camera quantification was performed on one of the deceased patients. Several isolated lesions were identified that were suitable for complete excision and could be used for the evaluation. Gamma camera imaging was performed on the excised humerus and part of the skull, both of which contained well-isolated lesions. The sites of high uptake corresponded exactly with visually identifiable areas of the samples, which were microscopically confirmed as metastases. Typically, these areas had osteoblastic activity interspersed with tumor cells. Finally, absolute activity calculations were performed on these samples, using a well counter. A comparison could be made between the three values thus obtained.

**Well Counter.** Samples taken from the autopsy were counted in a calibrated NaI(Tl) well counter. The lesions were clearly visible, usually as lighter-colored areas. Samples were carefully cut from these areas using a scalpel. Care was taken not to include unwanted bone in any sample. The hard cortical bone was cut using a fine-toothed saw. The well counter had a 2-in. crystal and was connected to a PC-based multichannel analyzer. The mass and activity were determined for complete lesions as well as for small samples taken from various sites within normal bone and lesions. The values from the gamma camera quantification were compared with these measurements.

**Autoradiography.** Autoradiography was performed in two ways. The activity distribution in large samples, for example, sections of the spinal column and humerus, was determined by filing a sawed-through section to create a flat surface. These flat sections were then placed in contact with the film (Agfa Structurix), which, in turn, was protected from moisture by a thin plastic wrapping. Exposure times were determined through trial and error.

To view the microscopic distribution, cryosections of  $30\ \mu\text{m}$  were made through various lesions. These sections were allowed to dry and placed in direct contact with the film in a film cassette. In this way, high-quality images of the distribution were obtained.

### Dose Calculations

Dose calculations were performed on a macroscopic level based on the MIRD formulation (5,14) and using the activity estimates from the gamma camera quantification. For the microscopic dose estimations, dose kernels (15,16) were used combined with the distribution information of the autoradiography.

**Macroscopic Dose Calculations.** Only the physical half-life of  $^{153}\text{Sm}$  was considered in calculating the cumulated activity needed in the MIRD dose calculation. It was assumed that the uptake, which was completed in 4 hr, and the biological half-life were

negligible (3,5,17). Specific absorbed fraction was taken as 1 for the nonpenetrating radiation, whereas that of the gamma radiation was calculated based on the size of the ROI used for determining the activity. The density of normal bone was assumed to be  $1.2\ \text{g}/\text{cm}^3$ , whereas that of the metastases was taken as  $1.5\ \text{g}/\text{cm}^3$ , based on actual measurements.

The dose is expressed as the absolute dose for a specific sample and also as dose per activity administered per ideal weight (kg). This value, expressed as  $\text{cGy} \cdot \text{kg}/\text{MBq}$ , can then be used to estimate the activity to be administered for a specific dose to normal bone or to the lesions.

**Microscopic Dose Calculations.** Average microscopic pictures of cortical and trabecular bone as well as osteoblastic lesions were used. A single cavity embedded in the average case was evaluated with the assumption that the activity was evenly distributed on the surface of the mineralized component. The models were:

1. Cortical bone: the mineralized bone was set at  $1000\ \mu\text{m}$ , and the canal was set at  $100\ \mu\text{m}$  wide;
2. Trabecular bone: because there are much greater fluctuations in the structure of trabecular bone, the mineralized component or trabeculae was assumed to be  $200\ \mu\text{m}$  wide, but cavities of  $500$ ,  $1000$  and  $1500\ \mu\text{m}$  were evaluated (however, these cavities were assumed to be surrounded by the average  $500\text{-}\mu\text{m}$  cavities); and
3. Osteoblastic lesion: the cavity was set at  $500\ \mu\text{m}$ , and the mineralized part was taken as  $200\ \mu\text{m}$ .

The dosages in the cavities were subsequently calculated and expressed as percentage of the macroscopic dosage. Both the kernels calculated by Simpkin and Mackie (16) and Johnson et al. (15) were used.

## RESULTS

### Calibration of the Channel Ratio Quantification Technique

**Attenuation Curve Measurement.** The shape of the attenuation curves, depicted in Figure 1, depends on both the size of the source and the positioning of the window. The curve has a smaller shoulder (less scatter) for the higher-energy window. This is exactly why the CR technique works. The fraction decreases more rapidly for the small source when compared to the larger source, again due to a reduced effect of the scatter.

**G and H Values.** The mean intrinsic G values varied from study to study, according to the tuning of the camera. The windows were positioned to give a value close to 1 in all instances. The maximum variation across the face of the camera was 2.3%.

The value of H depends on the value of G, source size and depth, and therefore, it is not truly a constant, as postulated. However, small changes in H, typically from 2.4 to 3.4, do not have a significant effect on quantification itself, and therefore, an average value of 2.9 was used throughout.

**Phantom Study.** The phantom thicknesses, as measured with a pair of calipers, were typically between 1 and 2 cm thinner than the equivalent thicknesses determined with the  $^{57}\text{Co}$  source.

The percentage differences between actual activity and measured activity are given in Table 1. The sensitivity of the camera remained constant at  $49.8\ \text{cts}/\text{MBq} \cdot \text{sec}$  (s.d. =  $2.6\ \text{cts}/\text{MBq} \cdot \text{sec}$ ).

### Patient Measurements

The patients consisted of four prostate cancer patients and one lung adenosquamous cancer, all of whom had developed bone metastases. Two prostate cancer patients received  $56\ \text{MBq}/\text{kg}$ , and the rest received  $111\ \text{MBq}/\text{kg}$  (activity injected divided by ideal body mass).

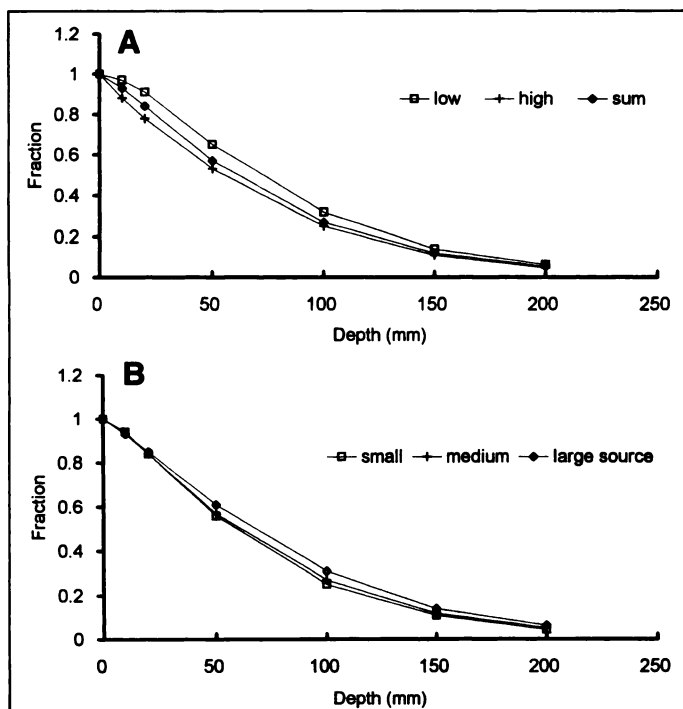


FIGURE 1. Attenuation curves for  $^{153}\text{Sm}$ . (A) Variation with window positioning. (B) Variation with source size.

The activity concentrations, expressed as MBq/g, in the samples for normal bone are given in Table 2. The main contributor to uncertainty in concentration is the estimation of mass of the sample. Not only is it difficult to determine the volume from planar images, but the samples may not be solid.

Table 3 lists the corresponding results for lesions. The estimation of the mass of the vertebrae lesions is fraught with difficulty because of the diffuse nature of the lesion.

### Postmortem Investigations

**Gamma Camera.** Figure 2 is a composite of  $^{153}\text{Sm}$ -EDTMP scans performed postmortem for one of the subjects. Figure 3 is a gamma camera image of the humerus removed at the autopsy. The results of three different methods are tabulated in Table 4.

**Well Counter.** The results of the well counter measurements are given in Table 5.

**Autoradiography.** A collage of autoradiographic images is shown in Figure 4.

### Dose Calculations

**Macroscopic Dosages.** The calculated dosages to normal bone and the lesions are given in Tables 2 and 3, respectively.

**Microscopic Dosages.** Due to the small size of the Haversian canals in cortical bone, the radiation in these canals is quite uniform. However, the dosage is higher than the average macroscopic dosage. The results show that the dosage is 292% of the average dosage at the surface of the canal and 215% in the middle.

TABLE 1

Percentage Difference between Actual and Measured Activity

Source	Sample no.			Average
	1	2	3	
Lumbar 1	7.3	-6.2	0.3	0.5
Lumbar 2	9.3	-0.2	0.2	3.1
Femur 1	14.0	-6.3	5.0	4.2
Femur 2	21.0	-4.3	9.6	8.8
Average	12.9	-4.3	3.8	4.1
s.d.				8.1

TABLE 2  
Activity and Radiation Dose in Normal Bone

Sample no.	Description	Concentration (MBq/g)	Dose (cGy)	Dose/activity injected* (cGy · kg/MBq)
1	Femur shaft	0.105	101	0.91
2	Femur head	0.194	187	1.7
3	Humerus shaft	0.109	105	1.9
4	Vertebrae	0.226	218	3.9
5	Hip	0.221	213	1.9

\*Samples came from different subjects. The administered activity was 56 MBq/kg for sample nos. 3 and 4, and for the rest, it was 111 MBq/kg.

To graphically illustrate the variation across a cavity, the spatial variation within a trabecular cavity is shown in Figure 5. Table 6 summarizes the results for the various scenarios for trabecular bone.

The results of the calculations for osteoblastic lesions were 61.5% and 585% for the data from Johnson et al. (15) and 85.0% and 162% for the data from Simpkin and Mackie (16) in the center and surface, respectively.

### DISCUSSION

#### Calibration of the Channel Ratio Quantification Technique

The differences between measured and equivalent thicknesses can be explained by considering that the bony structures are more dense than water and, therefore, add to the equivalent thickness.

It was heartening to see that the camera sensitivity remained constant with time. The accuracy of the study was, on average, 4.1%, with a s.d. of 8.1%. This error would, therefore, also be introduced into the radiation dosage estimates, but it was small enough to allow sensible deductions to be made.

#### Patient Measurements

The results show that areas with a higher trabecular bone content have higher concentrations of activity. This is easily explained because there is more surface area available for the activity to attach to than is the case with cortical bone. Better perfusion would also ensure a higher supply of activity.

Note that, although there are large fluctuations in the value of the ratio, the absolute activity concentration for trabecular bone is  $\sim 0.22$  MBq/g and that of cortical bone is  $\sim 0.1$  MBq/g. This may indicate that a ceiling in the uptake in normal bone will be reached if the administered activity is in excess of 56 MBq/kg (the lowest limit in this study). The exact limit cannot be gleaned from our limited range. We are currently investigating this postulate.

As in the results found for healthy bone, activity concentrates more in the lesions within trabecular bone. The activity con-

TABLE 3  
Activity and Dose in Lesions

Sample no.	Description	Concentration (MBq/g)	Dose (cGy)	Dose/activity injected (cGy · kg/MBq)
1	Femur lesion	0.738	712	6.4
2	Hip lesion	1.413	1364	12.3
3	Vertebrae lesion	1.396	1347	12.1
4	Hip lesion	1.457	1407	12.7
5	Humerus lesion	0.300	290	5.2
6	Skull lesion	0.843	814	14.5
7	Vertebrae lesion	1.572	1517	27.1

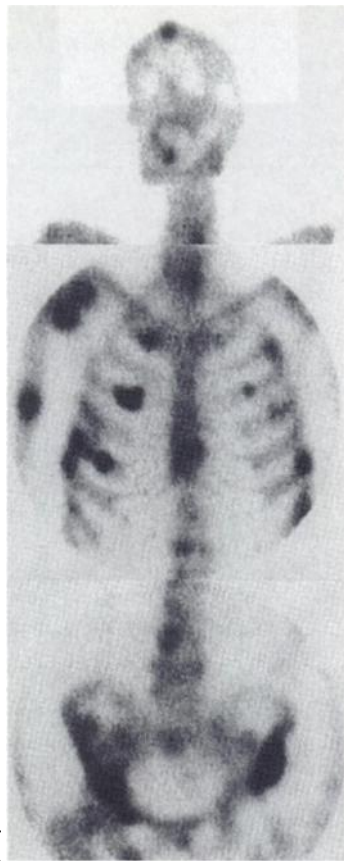


**FIGURE 2.** Composite  $^{153}\text{Sm}$ -EDTMP scan performed postmortem.

centration ratio is between 3 and 7 times higher in the lesions as compared to their corresponding healthy bone. If a ceiling exists for lesions, it is higher than at the levels of this study.

#### Postmortem Investigation

The gamma camera investigation confirmed the accuracy of quantification. The correlation between the various techniques was excellent. The activity concentrations, as determined by the accurate well counter measurements, followed the same pattern that was observed in the *in vivo* study.

The autoradiographic evaluation reveals that the activity is exclusively associated with the surface of the bone's internal structures. It also closely correlates with the perfusion pattern within the bone and lesions. One would typically find increased

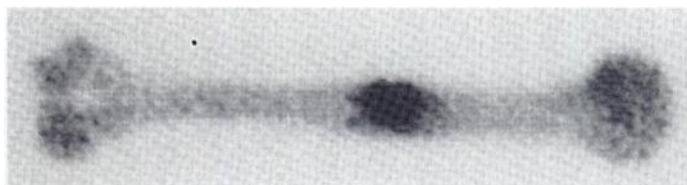


**FIGURE 3.** Gamma camera image of humerus removed at autopsy.

**TABLE 4**  
Comparison of Activity Measurements

Sample description	Well counter	Body section*	Sample*
Humerus lesion	23.5	24.5	28.7
Healthy humerus	5.4	5.8	4.9
Skull lesion	10.8	10.9	11.0

Measurements are in MBq.

\*Determined using a gamma camera.

**TABLE 5**  
Activity Concentrations of Excised Sample

Sample description	Mass (g)	Activity concentration (MBq/g)
Trabecular bone 1	1.11	0.237
Trabecular bone 2	0.85	0.197
Cortical bone 1	1.37	0.160
Cortical bone 2	0.93	0.026
Vertebral metastasis 1	1.94	1.482
Vertebral metastasis 2	1.16	2.649
Vertebral metastasis 3	1.1	2.752
Vertebral metastasis 4	2.29	2.652
Human lesion marrow 1	0.34	0.180
Human lesion marrow 2	0.32	0.124
Cortical lesion	0.58	0.359
Skull lesion 1	0.15	0.683
Skull lesion 2	0.08	0.902

uptake immediately adjacent to the blood vessels. Activity distribution is therefore not uniform throughout the bone or the lesions. The nonuniformity is slightly more pronounced in the second case, in which the lesions are of an osteolytic nature.

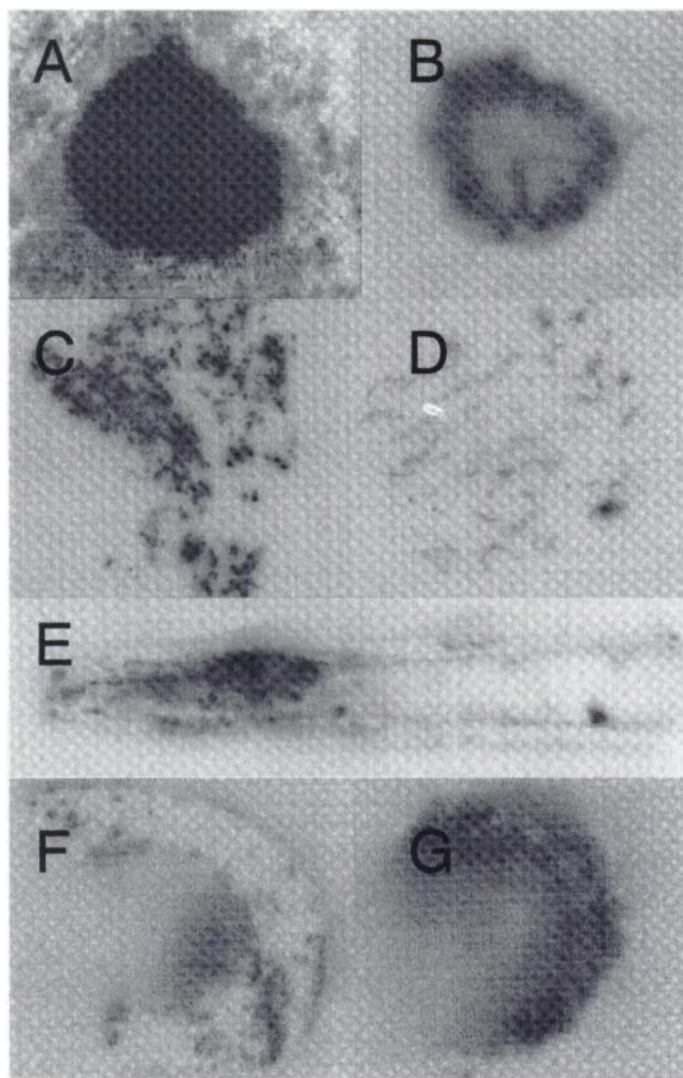


**FIGURE 4.** Results of autoradiography. (A) Skull lesion exposed for normal bone. (B) Skull lesion exposed for metastasis. (C) Trabecular metastasis. (D) Normal trabecular bone. (E) Oblique slice through humerus at level of lesion. (F) Cross-section through normal humerus. (G) Cross-section through lesion in humerus. Magnification varies throughout the panels.

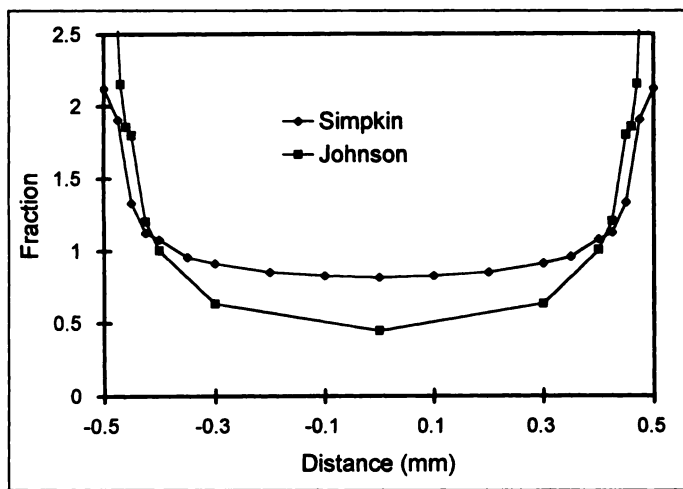


FIGURE 5. Microscopic dose distribution across 1000- $\mu$ m trabecule, compared to macroscopic dose.

### Dose Calculations

**Macroscopic Dosages.** The dose to normal bone per activity administered varies between 0.9 and 3.9 cGy  $\cdot$  kg/MBq. When 28 MBq/kg is administered, as is the case of the estimates by Logan et al. (5), the dosage to normal bone will be between 25 and 109 cGy. This value is much lower than estimates based on the work of Logan et al. (5). In their estimation, a dose of 330 cGy would be expected. They assumed that 90% of the activity is retained and uniformly distributed throughout the skeleton. Our results therefore imply that <33% of the retained activity may be found in normal bone and that the remaining activity will be in the lesions.

As expected, the dosage to the lesions is considerably higher than that of normal bone. The dosages are, however, not high enough to ensure sterilization of the lesions.

**Microscopic Dosages.** Because the activity coats the surface of the bone, the radiation dose in the cavities varies considerably. In normal bone, this works to our advantage because bone marrow in the center of a trabecule would be spared. However, by the same token, malignant cells could also survive if they

TABLE 6  
Percentage Dosages in Trabecular Cavities

Cavity ( $\mu$ m)	Johnson et al. (15)		Simpkin and Mackie (16)	
	Center	Surface	Center	Surface
500	102	965	127	241
1000	44.5	937	74.1	200
1500	14.9	297	44.9	184

were not near the bone surface. Sterilization of a lesion will therefore not be feasible in large lesions in which these cells are out of the effective reach of the radiation. The pain-causing mechanisms are linked to bone formation, which takes place exclusively at the sites of high activity uptake, thus ensuring the efficacy of this treatment.

### CONCLUSION

Quantification could be performed accurately, and the distribution of the activity was determined at the microscopic level. The radiation dosages to the various structures were calculated based on actual measurements rather than assumptions.

The clinically observed effects can now be explained. The lower than expected toxicity is due to an overestimation of the amount of activity taken up by normal bone, compounded by the surface distribution within the bone. The net effect is a lower than expected radiation dose to the bone marrow. The large variation in the dosage when viewed microscopically explains why the pain returns within a few weeks. Current schedules would not result in the sterilization of the lesions.

### REFERENCES

- Turner HJ, Claringbold PG. A Phase II study of treatment of painful multifocal skeletal metastases with single and repeated dose samarium-153-EDTMP. *Eur J Cancer* 1991;27:1084-1086.
- Collins C, Eary JF, Donaldson G, et al. Samarium-153-EDTMP in bone metastases of hormone refractory prostate carcinoma: a Phase III trial. *J Nucl Med* 1993;34:1839-1844.
- Farhanghi M, Holmes RA, Volkert WA, Logan KW, Singh A. Samarium-153-EDTMP: pharmacokinetics, toxicity and pain response using an escalating dose schedule in treatment of metastatic bone cancer. *J Nucl Med* 1992;33:1451-1458.
- Lewington VJ. Cancer therapy using bone-seeking isotopes. *Phys Med Biol* 1996;41:2027-2042.
- Logan KW, Volkert WA, Holmes RA. Radiation dose calculation in persons receiving injections of samarium-153-EDTMP. *J Nucl Med* 1987;28:505-509.
- Heggie JCP. Radiation absorbed dose calculations for samarium-153-EDTMP localized in bone. *J Nucl Med* 1991;32:840-844.
- Eary JF, Collins C, Stabin M, et al. Samarium-153-EDTMP biodistribution and dosimetry estimation. *J Nucl Med* 1993;34:1031-1036.
- van Rensburg AJ, Lötter MG, van Aswegen A, et al. A new scatter correction technique for radionuclide image quantitation. *J Nucl Med* 1992:888.
- Pretorius PH, van Rensburg AJ, van Aswegen A, et al. The channel ratio method of scatter correction for radionuclide image quantitation. *J Nucl Med* 1993;34:330-335.
- Sgouros G, Basset G, Thekkumthala G, et al. Treatment planning for internal radionuclide therapy: three dimensional dosimetry for nonuniformly distributed radionuclides. *J Nucl Med* 1990;31:1884-1891.
- Giap HB, Macey DJ, Podoloff DA. SPECT-based three dimensional treatment planning system for radio-immunotherapy. *J Nucl Med* 1995;36:1885-1894.
- van Rensburg AJ, Lötter MG, Heyns A du P, et al. An evaluation of four methods of <sup>111</sup>In planar image quantification. *Med Phys* 1988;15:853-861.
- Albert AS, Smit BJ, Louw WKA, van Rensburg AJ, et al. The dose response relationship and multiple dose efficacy and toxicity of samarium-153-EDTMP in metastatic cancer to bone. *Radiother Oncol* 1997;43:175-179.
- Loevinger R, Budinger TE, Watson EE. *MIRD primer for absorbed dose calculations*. New York: The Society of Nuclear Medicine; 1991:25-3.
- Johnson JC, Langhorst SM, Loyalka SK, et al. Calculation of radiation dose at a bone-to-marrow interface using Monte Carlo modeling techniques (EGS4). *J Nucl Med* 1992;33:623-628.
- Simpkin DJ, Mackie TR. EGS4 Monte Carlo determination of the beta dose kernel in water. *Med Phys* 1990;17:179-186.
- Louw WK, Dormehl IC, van Rensburg AJ, et al. Evaluation of samarium-153 and holmium-166-EDTMP in the normal baboon model. *Nucl Med Biol* 1996;23:935-940.